Use this document as a template

Millikelvin Confocal Microscopy of Semiconductor Membranes and Filter Functions for Unital Quantum Operations

Customise this page according to your needs

Tobias Hangleiter[*]

July 18, 2025

[*] A LaTeX lover/hater

The harmony of the world is made manifest in Form and Number, and the heart and soul and all the poetry of Natural Philosophy are embodied in the concept of mathematical beauty.

– D'Arcy Wentworth Thompson

Contents

List of Figures

Publications

[1] Yaiza Aragonés-Soria, René Otten, Tobias Hangleiter, Pascal Cerfontaine, and David Gross. "Minimising Statistical Errors in Calibration of Quantum-Gate Sets." June 7, 2022. DOI: 10.48550/arXiv.2206.03417. (Visited on 06/08/2022). Pre-published.

[2] Pascal Cerfontaine, Tobias Hangleiter, and Hendrik Bluhm. "Filter Functions for Quantum Processes under Correlated Noise." In: *Phys. Rev. Lett.* 127.17 (Oct. 18, 2021), p. 170403. DOI: 10.1103/PhysRevLett.127.170403.

[3] Thomas Descamps, Feng Liu, Sebastian Kindel, René Otten, Tobias Hangleiter, Chao Zhao, Mihail Ion Lepsa, Julian Ritzmann, Arne Ludwig, Andreas D. Wieck, Beata E. Kardynał, and Hendrik Bluhm. "Semiconductor Membranes for Electrostatic Exciton Trapping in Optically Addressable Quantum Transport Devices." In: *Phys. Rev. Appl.* 19.4 (Apr. 28, 2023), p. 044095. DOI: 10.1103/PhysRevApplied.19.044095. (Visited on 04/28/2023).

[4] Thomas Descamps, Feng Liu, Tobias Hangleiter, Sebastian Kindel, Beata E. Kardynał, and Hendrik Bluhm. "Millikelvin Confocal Microscope with Free-Space Access and High-Frequency Electrical Control." In: *Rev. Sci. Instrum.* 95.8 (Aug. 9, 2024), p. 083706. DOI: 10.1063/5.0200889. (Visited on 08/12/2024).

[5] Denny Dütz, Sebastian Kock, Tobias Hangleiter, and Hendrik Bluhm. "Distributed Bragg Reflectors for Thermal Isolation of Semiconductor Spin Qubits." In preparation.

[6] Sarah Fleitmann, Fabian Hader, Jan Vogelbruch, Simon Humpohl, Tobias Hangleiter, Stefanie Meyer, and Stefan van Waasen. "Noise Reduction Methods for Charge Stability Diagrams of Double Quantum Dots." In: *IEEE Trans. Quantum Eng.* 3 (2022), pp. 1–19. DOI: 10.1109/TQE.2022.3165968.

[7] Fabian Hader, Jan Vogelbruch, Simon Humpohl, Tobias Hangleiter, Chimezie Eguzo, Stefan Heinen, Stefanie Meyer, and Stefan van Waasen. "On Noise-Sensitive Automatic Tuning of Gate-Defined Sensor Dots." In: *IEEE Trans. Quantum Eng.* 4 (2023), pp. 1–18. DOI: 10.1109/TQE.2023.3255743.

[8] Tobias Hangleiter, Pascal Cerfontaine, and Hendrik Bluhm. "Filter-Function Formalism and Software Package to Compute Quantum Processes of Gate Sequences for Classical Non-Markovian Noise." In: *Phys. Rev. Research* 3.4 (Oct. 18, 2021), p. 043047. DOI: 10.1103/PhysRevResearch.3.043047. (Visited on 01/19/2022).

[9] Tobias Hangleiter, Pascal Cerfontaine, and Hendrik Bluhm. "Erratum: Filter-function Formalism and Software Package to Compute Quantum Processes of Gate Sequences for Classical Non-Markovian Noise [Phys. Rev. Research 3, 043047 (2021)]." In: *Phys. Rev. Res.* 6.4 (Oct. 16, 2024), p. 049001. DOI: 10.1103/PhysRevResearch.6.049001. (Visited on 10/16/2024).

[10] Isabel Nha Minh Le, Julian D. Teske, Tobias Hangleiter, Pascal Cerfontaine, and Hendrik Bluhm. "Analytic Filter-Function Derivatives for Quantum Optimal Control." In: *Phys. Rev. Applied* 17.2 (Feb. 2, 2022), p. 024006. DOI: 10.1103/PhysRevApplied.17.024006. (Visited on 02/03/2022).

[11] Paul Surrey, Julian D. Teske, Tobias Hangleiter, Pascal Cerfontaine, and Hendrik Bluhm. "Data-Driven Qubit Characterization and Optimal Control Using Deep Learning." In preparation.

[12] Kui Wu, Sebastian Kindel, Thomas Descamps, Tobias Hangleiter, Jan Christoph Müller, Rebecca Rodrigo, Florian Merget, Beata E. Kardynal, Hendrik Bluhm, and Jeremy Witzens. "Modeling an Efficient Singlet-Triplet-Spin-Qubit-to-Photon Interface Assisted by a Photonic Crystal Cavity." In: *Phys. Rev. Appl.* 21.5 (May 24, 2024), p. 054052. DOI: 10.1103/PhysRevApplied.21.054052. (Visited on 08/21/2024).

[13] Kui Wu, Sebastian Kindel, Thomas Descamps, Tobias Hangleiter, Jan Christoph Müller, Rebecca Rodrigo, Florian Merget, Hendrik Bluhm, and Jeremy Witzens. "An Efficient Singlet-Triplet Spin Qubit to Fiber Interface Assisted by a Photonic Crystal Cavity." In: *25th Eur. Conf. Integr. Opt.* Ed. by Jeremy Witzens, Joyce Poon, Lars Zimmermann, and Wolfgang Freude. Cham: Springer Nature Switzerland, 2024, pp. 365–372. DOI: 10.1007/978-3-031-63378-2_60.

Software

The following open-source software packages were developed (at least partially) during the work on this thesis.

[1] Tobias Hangleiter, Isabel Nha Minh Le, and Julian D. Teske, *Filter_functions* version v1.1.3, May 14, 2024. Zenodo. DOI: 10.5281/ZENODO.4575000.

[2] Tobias Hangleiter, *Lindblad_mc_tools*.

[3] Tobias Hangleiter, *Mjolnir*.

[4] Tobias Hangleiter, Simon Humpohl, Max Beer, and René Otten, *Python-Spectrometer* version 2024.11.1, Nov. 21, 2024. Zenodo. DOI: 10.5281/ZENODO.13789861.

[5] Tobias Hangleiter, Simon Humpohl, Paul Surrey, and Han Na We, *Qutil* version 2024.11.1, Nov. 21, 2024. Zenodo. DOI: 10.5281/ZENODO.14200303.

Part I

A Flexible Python Tool For Fourier-Transform Noise Spectroscopy

Part II

Characterization and Improvements of a Millikelvin Confocal Microscope

Part III

Optical Measurements of Electrostatic Exciton Traps in Semiconductor Membranes

Introduction | 2

C ATS

Photoluminescence and excitons in semiconductors 3

RATS The effective masses of the holes along the growth-direction are

$$m^*_{hh,z} = \frac{1}{\gamma_1 - 2\gamma_2} = 0.38 \tag{3.1}$$

$$m^*_{lh,z} = \frac{1}{\gamma_1 + 2\gamma_2} = 0.09 \tag{3.2}$$

with

$$\gamma_1 = 6.8 \tag{3.3}$$
$$\gamma_2 = 2.1. \tag{3.4}$$

In-plane, the masses then become

$$m^*_{hh,\|} = \frac{1}{\gamma_1 + \gamma_2} = 0.11 \tag{3.5}$$

$$m^*_{lh,\|} = \frac{1}{\gamma_1 - \gamma_2} = 0.21 \tag{3.6}$$
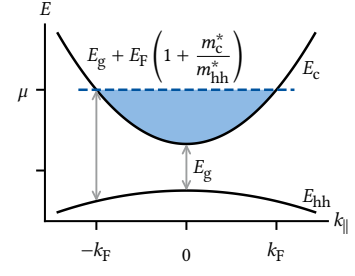
Figure 3.1: Band structure diagram of a doped heterostructure (after Reference 1). Due to the *n*-type doping, the conduction band is filled up to the Fermi level μ. Photonic excitation of an electron-hole pair can only occur at $|k| > k_F$ into the free states above μ due to the small photon momentum. Recombination can occur within a bandwidth of $E_F(1 + m_c^*/m_{hh}^*)$.
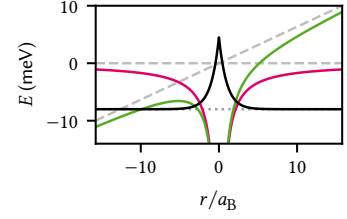
Figure 3.2: Effect of an in-plane electric field on an exciton wavefunction. In the hole's reference frame, the electron sees a static attractive Coulomb potential (magenta), resulting in a bound state (dotted gray line, wave function sketched in black). Applying an electric field ($F = 100\,\text{mV}/\mu\text{m}$, dashed gray lines) tilts the Coulomb potential (green) and leads to a transparent barrier through which the electron can tunnel out.

3.1 The quantum-confined Stark effect

In order to obtain a qualitative understanding of the influence of an electric field on the photoluminescence (PL), consider an undoped GaAs/Al$_{0.33}$Ga$_{0.66}$As quantum well (QW) of width $L = 20$ nm. We take a 57:43 ratio for the band offsets [2], resulting in discontinuities of height $\Delta E_c = 0.24$ eV and $\Delta E_{hh} = 0.18$ eV at the interfaces for the conduction and the heavy-hole valence band, respectively, and $m_c^*/m_e = 0.067$ and $m_{hh}^*/m_e = 0.34$ for the effective masses.[1] Assuming an infinitely deep well for simplicity, the eigenenergies are

$$E_n = \frac{1}{2m^*}\left[\frac{\pi\hbar n}{L}\right]^2 \tag{3.7}$$

and the eigenstates are

$$\psi_n(z) = \sqrt{\frac{2}{L}}\sin\left(\frac{n\pi z}{L}\right). \tag{3.8}$$

The ground state energy is then 14 meV (3 meV) above the band edge, corresponding to 6 % (2 %) of the respective band offsets and implying that the infinite-well approximation is acceptable.[2] The upper panel of Figure 3.1 depicts the first two wavefunctions of electrons and holes in a band structure diagram. Due to the symmetry of the confining potential, the wavefunctions are symmetric around the center of the well.

Now, applying an out-of-plane electric field tilts the bands and pulls electrons and holes to opposite interfaces of the QW. The Hamiltonian for the electrons in this case reads [3–5]

$$H = -\frac{\hbar^2}{2m^*}\frac{d^2}{dz^2} + eFz \tag{3.9}$$

if we take z to be zero at an interface and choose $F \geq 0$. Introducing the length and energy scales [5]

$$\tilde{\epsilon} = \left[\frac{(\hbar eF)^2}{2m^*}\right]^{\frac{1}{3}}, \tag{3.10}$$

$$\tilde{z} = \left[\frac{\hbar^2}{2m^*eF}\right]^{\frac{1}{3}} = \frac{\tilde{\epsilon}}{eF}, \tag{3.11}$$

and defining

$$Z_n = z/\tilde{z} - \epsilon_n/\tilde{\epsilon} \tag{3.12}$$

with ϵ_n the eigenenergy, the Schrödinger equation becomes [3]

$$\frac{d^2}{dZ_n^2}\psi_n(Z_n) = Z_n\psi_n(Z_n). \tag{3.13}$$

Equation 3.13 is known as the Stokes or Airy equation and has the general solution

$$\psi_n(Z_n) = \alpha_n\,\text{Ai}(Z_n) + \beta_n\,\text{Bi}(Z_n), \tag{3.14}$$

where Ai(z) and Bi(z) are the Airy functions. The Ai(z) and Bi(z) oscillate for $z < 0$ and decay (grow) exponentially for $z > 0$, respectively. As we assumed infinitely high barriers at $z = 0$ and $z = L$, the boundary conditions impose

$$\psi_n(0) = \psi_n(L) = 0, \tag{3.15}$$

which completely determines the eigenstates and -energies. For large

1: I note that the literature knows many different values for the hole effective mass in the plane of a quantum well, suggesting that one should actually measure it to be confident in the actual value.

2: In a finite well, the wavefunctions decay exponentially into the barriers and result in slightly lower eigenenergies. However, the qualitative behavior remains the same.
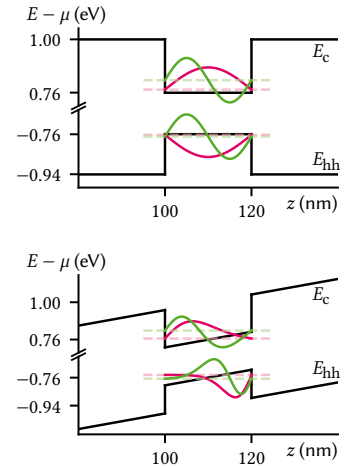
Figure 3.3: Quantum-confined Stark effect (QCSE) in an undoped QW. Top: conduction and heavy-hole valence band profiles along the growth direction. The wavefunctions of the first two eigenstates in the well are drawn in magenta and green, respectively. The ground state transition is larger by $\Delta E = 17$ meV than the gap E_g due to the confinement. Bottom: same structure as above with an out-of-plane electric field applied across the structure ($F = 5$ V/µm). Analytical wavefunctions in the infinite-well approximation are shown in magenta and green again. The wavefunctions get pushed to opposite interfaces of the QW, lowering the ground state transition energy by $\Delta E = -10$ meV. Excitonic effects are not included.

well widths or fields ($eFL/\epsilon_n \gg 1$), the second term is exponentially suppressed and the eigenenergies are given by the zeros of $\mathrm{Ai}(Z_n)$. For zero field, one recovers the square well solution (Equations 3.7 and 3.8).

The finite-field case is shown in the lower panel of Figure 3.1 for $F = 5\,\mathrm{V}/\mu\mathrm{m}$. Due to the larger effective mass of the heavy holes, the characteristic length scale $\tilde{z}$ is shorter and hence the corresponding wavefunctions are narrower than their electronic counterparts. The ground state transition energy at this field is $10\,\mathrm{meV}$ below the gap or $27\,\mathrm{meV}$ lower than in the zero-field case.

For a full quantitative accounting of the transition energies, the exciton binding energy as well as finite barrier heights would be required. The former is on the order of $6\,\mathrm{meV}$ to $9\,\mathrm{meV}$ in GaAs and becomes smaller as the overlap of the electron and hole wavefunctions is reduced when applying an electric field, pulling the wavefunctions to opposite interfaces. Miller et al. [4] found that finite-well properties could be reproduced by using effective well widths with infinite well models.

The latter should have a small effect on the ground state energy as argued above. Additionally, tilting the QW results in a finite probability for the charge carriers confined within the well to escape as – for infinitely thick barriers – lower-lying states become available at some distance away, an effect known as Fowler-Nordheim tunneling. Following Reference 5, we can estimate the tunneling probability as

$$\mathscr{T}_n(F) \approx \exp\left\{ -\frac{\sqrt{4m^*(\Delta E_{\mathrm{c(hh)}} - \epsilon_n)^3}}{eF\hbar} \right\}, \qquad (3.16)$$

where $\Delta E_{\mathrm{c(hh)}}$ is the conduction (valence) band offset.

3.1.1 In-plane confinement

So far, we have considered the QCSE in a single dimension, as if we were to apply a global electric field. However, as we saw before, the field lowers the exciton energy below the QW confinement and hence, if applied locally, results in an effective confinement potential in the plane of the QW. Descamps [6] performed numerical simulations for a geometry with circular gate electrodes with $200\,\mathrm{nm}$ diameter on both sides of a membrane, finding a confinement depth of $20\,\mathrm{meV}$ at $F = 5\,\mathrm{V}/\mu\mathrm{m}$ that is well approximated by a single-particle harmonic potential with confinement strength $\omega/2\pi = 738\,\mathrm{GHz}$ corresponding to an oscillator length $\xi = \sqrt{\hbar/M\omega} = 20\,\mathrm{nm}$.

How does this in-plane confinement modify the wavefunction? The harmonic potential applies to the center-of-mass wavefunction of the exciton with mass $M = m_{\mathrm{c}}^* + m_{\mathrm{hh}}^*$. We ignore the relative motion of electron and hole as the optical properties of the exciton are dominated by the behavior at zero separation for $a_{\mathrm{B}}/\xi < 1$ [7], where $a_{\mathrm{B}} = 2\pi\epsilon_0\epsilon_r\hbar^2/\mu e^2 = 6\,\mathrm{nm}$ is the exciton Bohr radius in two dimensions with $\epsilon_r = 13.3$ in GaAs at low temperatures and μ the reduced effective mass [8], and consider only $\Delta n = 0$ transitions, *i.e.*, electron and hole in the same z quantum state, as $\Delta n \neq 0$ transitions are much weaker [5]. Let us further initially assume a separable wavefunction and choose cylindrical coordinates according to the symmetry of the potential. We then have

$$\Psi_{np\ell}(z_e, z_h, \rho, \phi) = \psi_n(z_e)\psi_n(z_h)\chi_{p\ell}(\rho)\exp(i\ell\phi) \qquad (3.17)$$
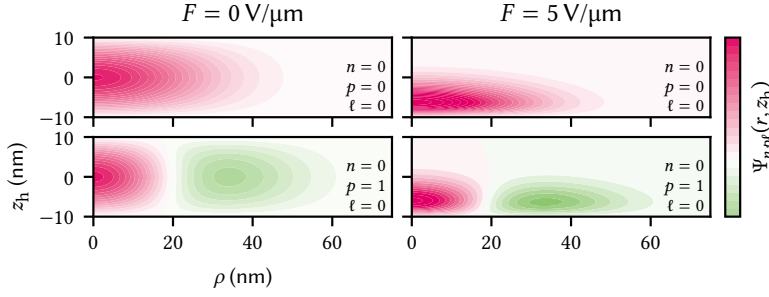
where [9][3]

$$\chi_{p\ell}(\rho, \phi) = \sqrt{\frac{2p!}{2\pi\xi^2(p + |\ell|)!}} \exp(-\tilde{\rho}^2/2)\tilde{\rho}^{|\ell|}L_p^{|\ell|}(\tilde{\rho}) \qquad (3.18)$$

with the associated Laguerre polynomial $L_p^{|\ell|}(x)$ and we used the shorthand $\tilde{\rho} = \rho/\xi$. The numbers $p \in \mathbb{N}$ and $\ell \in \mathbb{Z}$ denote the principal and orbital momentum quantum numbers. The eigenenergies of the harmonic oscillator solution Equation 3.18 are given by

$$\epsilon_{p\ell} = \hbar\omega(2p + |\ell| + 1). \qquad (3.19)$$

To account for a finite well width ($L \approx \xi$ in our case), we can to a first approximation perform the replacement $\rho \rightarrow r = \sqrt{\rho^2 + z^2}$ in Equation 3.17. The resulting wavefunction $\Psi_{np\ell}(r, z_{\mathrm{h}})$ at fixed electron coordinate z_{e} is shown in Figure 3.4 for $n = \ell = 0$ (which makes it independent of ϕ).

At last, we can use the exciton wavefunction $\Psi_{nm\ell}(r, \phi, z_{\mathrm{e}}, z_{\mathrm{h}})$ to estimate the *oscillator strength*, a quantity often quoted in semiconductor spectroscopy. The oscillator strength puts in relation the quantum mechanical transition rate with the emission rate of a classical oscillator with frequency $\omega = \Delta E/\hbar$ [10]. For a dipole transition from state $|i\rangle$ to state $|j\rangle$, it may be written as [5]

$$f_{ji} = \frac{2\mu\Delta E_{ji}}{\hbar^2}|\langle j|\mathbf{r}|i\rangle|^2, \qquad (3.20)$$

where μ is the reduced mass of the exciton. As the selection rules only allow in-plane dipole transitions for heavy holes, we write [7]

$$f_{np\ell} = \frac{2\mu\Delta E_{np\ell}}{\hbar^2}J_r^2 J_\phi^2|\langle u_{\mathrm{c}}|x|u_{\mathrm{hh}}\rangle|^2 \qquad (3.21)$$

for transitions with $\Delta n = \Delta p = \Delta \ell = 0$, where

$$J_r = \int_0^L dz \int_0^\infty d\rho\, \rho\psi_n^{(\mathrm{e})}(z)\psi_n^{(\mathrm{h})}(z)\chi_{p\ell}(\sqrt{\rho^2 + z^2}), \qquad (3.22)$$

$$J_\phi = \int_0^{2\pi} d\phi\, \exp(i\ell\phi), \qquad (3.23)$$

and $|u_{\mathrm{c(hh)}}\rangle$ are the Bloch functions of the valence and conduction band, respectively, that we have neglected so far.

$\ell \neq 0$, $\Delta\epsilon_{p\ell} = 2p = 1$ meV (*cf.* Reference 6)
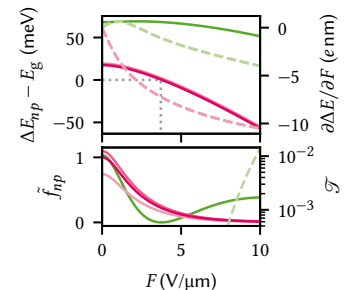
The `mjolnir` measurement framework │ 4

M JÖLNIR

```
├─ 📁 doc
├─ 📂 src
│   └─ 📂 mjolnir
│       ├─ 📂 config
│       │   ├─ 📄 physical_[…].yaml
│       │   ├─ 📄 optical_path.yaml
│       │   ├─ 📄 fig_F10.yaml
│       │   └─ 📄 …
│       ├─ 📂 instruments
│       │   ├─ 📄 __init__.py
│       │   ├─ 📄 logical_[…].py
│       │   └─ 📄 physical_[…].py
│       ├─ 📂 measurements
│       │   ├─ 📄 __init__.py
│       │   ├─ 📄 handler.py
│       │   ├─ 📄 measures.py
│       │   └─ 📄 sweeps.py
│       ├─ 📁 parameters
│       ├─ 📂 plotting
│       │   ├─ 📄 __init__.py
│       │   ├─ 📄 live_view.py
│       │   └─ 📄 plot_nd.py
│       ├─ 📄 __init__.py
│       ├─ 📄 calibration.py
│       └─ 📄 …
├─ 📄 main.py
├─ 📄 pyproject.toml
└─ 📄 …
```
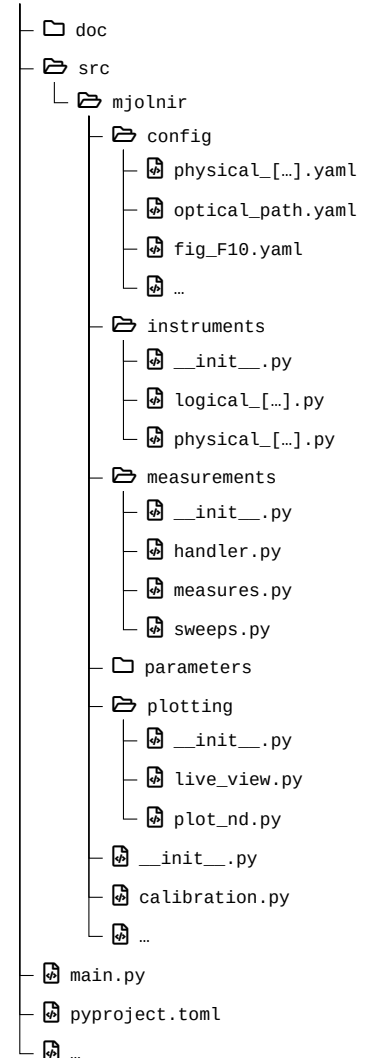
Figure 4.1: Source tree structure of the `mjolnir` package. Logical `QCoDeS` instruments and parameters are defined in the `instruments` and `parameters` modules, respectively. Instruments are configured using `yaml` files located in the `config` directory. The `measurements` module provides classes for the abstraction of measurements using `QCoDeS` underneath. Live plots of instrument data as well as a plot function for multidimensional measurement data are defined in the `plotting` module. `calibration.py` contains routines for power, CCD, and excitation rejection calibrations. The `main.py` file is a code cell-based script that serves as the entrypoint for measurements.

Observations | 5

P IDGEONS

5.1 Transfer-matrix method simulations of the membrane structure

The transfer-matrix method (TMM) is a computationally efficient method of obtaining the electric field in layered structures. In this section, I perform simulations of the heterostructure membranes investigated in this part of the present thesis using the PyMoosh package [11] to elucidate the observed quenching of PL when illuminating gate electrodes as well as the overall optical efficiency.[1] I will first briefly recap the simulation method following Reference 11. For more details, refer to *ibid.* and references therein.

Consider a layered structure along z with interfaces at $z_i, i \in \{0, 1, \dots, N+1\}$ that is translationally invariant along x and y. Each layer i may consist of a different dielectric material characterized by a (complex) relative permittivity $\epsilon_{r,i}$.[2] The electric field component along y of an electromagnetic wave transverse electric (TE) mode originating in some far away point satisfies the Helmholtz equation

$$\frac{\partial^2 E_y}{\partial z^2} + \gamma_i^2 E_y = 0, \tag{5.1}$$

where $\gamma_i = \sqrt{\epsilon_{r,i} k_0^2 - k_x^2}$ with $k_0 = \omega/c$ the wave vector in vacuum and k_x the component along x. In layer i of the structure, the solution to Equation 5.1 may be written as a superposition of plane waves incident and reflected on the lower and upper interfaces [11],

$$\begin{cases} E_{y,i}(z) = A_i^+ \exp\{i\gamma_i[z - z_i]\} + B_i^+ \exp\{-i\gamma_i[z - z_i]\}, \\ E_{y,i}(z) = A_i^- \exp\{i\gamma_i[z - z_{i+1}]\} + B_i^- \exp\{-i\gamma_i[z - z_{i+1}]\}, \end{cases} \tag{5.2}$$

where the coefficients with superscript $+$ $(-)$ are referenced to the phase at the upper (lower) interface, respectively. Matching these solutions at $z = z_i$ for all i to satisfy the interface conditions imposed by Maxwell's equations gives rise to a linear system of equations, the solution to which can be obtained through several different methods.

A particularly simple method is the transfer-matrix method (T-matrix formalism), which corresponds to writing the interface conditions at $z = z_i$ as the matrix equation

$$\begin{pmatrix} A_{i+1}^+ \\ B_{i+1}^+ \end{pmatrix} = T_{i,i+1} \begin{pmatrix} A_i^- \\ B_i^- \end{pmatrix} \tag{5.3}$$

with

$$T_{i,i+1} = \frac{1}{2\gamma_{i+1}} \begin{pmatrix} \gamma_i + \gamma_{i+1} & \gamma_i - \gamma_{i+1} \\ \gamma_i - \gamma_{i+1} & \gamma_i + \gamma_{i+1} \end{pmatrix} \tag{5.4}$$

the transfer matrix for interface i. Connecting the coefficients for adjacent interfaces within a layer of height $h_i = z_{i+1} - z_i$ requires propagating

<div style="float: right; width: 35%;">

1: Strictly speaking, the term TMM only refers to one of the several formalisms implemented in the PyMoosh package. While fast, it not the most numerically stable, and other methods may be preferred if wall time is not a limiting issue.

2: We disregard magnetic materials with relative permeability $\mu_r \neq 1$ for simplicity.

</div>

the phase,

$$\begin{pmatrix} A_i^- \\ B_i^- \end{pmatrix} = C_i \begin{pmatrix} A_i^+ \\ B_i^+ \end{pmatrix}, \tag{5.5}$$

with

$$C_i = \exp\{\operatorname{diag}(-i\gamma_i h_i, i\gamma_i h_i)\}. \tag{5.6}$$

Iterating Equations 5.4 and 5.6, the total transfer matrix $T = T_{0,N+1}$ then reduces to the matrix product

$$T = T_{N,N+1} \prod_{i=0}^{N-1} T_{i,i+1} C_i. \tag{5.7}$$

From T, the reflection and transmission coefficients can be obtained as $r = A_0^- = -T_{01}/T_{00}$ and $t = B_{N+1}^+ = rT_{10} + T_{11}$. Taking the absolute value square of reflection and transmission coefficients then yields the reflectance $\mathscr{R}$ and the transmittance $\mathscr{T}$, which correspond to the fraction of total incident power being reflected and transmitted, respectively. To obtain the absorptance $\mathscr{A}$, the fraction of power being absorbed, in layer i, one can compute the difference of the z-components of the Poynting vectors (*cf.* **??**) at the top of layers i and $i + 1$. In the TE case considered here, **??** reduces to [11]

$$S_i = \operatorname{Re}\left[\frac{\gamma_i^*}{\gamma_0}\left(A_i^+ - B_i^+\right)^*\left(A_i^+ + B_i^+\right)\right] \tag{5.8}$$

and is hence straightforward to extract from the calculation of either the S or T matrices.

Equation 5.7 is simple to evaluate on a computer, making this method attractive for numerical applications. However, the opposite signs in the argument of the exponentials in Equation 5.6 can lead to instabilities for evanescent waves ($\gamma_i \in \mathbb{C}$) due to finite-precision floating point arithmetic [12]. Rewriting Equation 5.4 to have incoming and outgoing fields on opposite sides of the equality alleviates this issue while sacrificing the simple matrix-multiplication composition rule in what is known as the scattering matrix (S-matrix) formalism. Finally, note that for a thorough accounting of in- and out-going field amplitudes, excitonic effects should be included, for example using the approach by D'Andrea and Del Sole [13].

Beyond the calculation of the aforementioned coefficients, the TMM formalism also allows to compute the full spatial dependence of the fields. Two cases are implemented in `PyMoosh`: irradiation of the layered structured with a Gaussian beam rather than plane waves of infinite extent, and a current line source inside the structure. In the first case, the previously assumed translational invariance along x leading to a plane-wave spatial dependence is replaced by a superposition of plane waves weighted with a normally distributed amplitude,[3]

$$E_{y,i}(x,z) = \exp(ik_x x) \to \int \frac{dk_x}{2\pi} \mathcal{E}_0(k_x) E_{y,i}(k_x, z) \exp(ik_x x), \tag{5.9}$$

with (*cf.* **??**)

$$\mathcal{E}_0(k_x) = \frac{w_0}{2\sqrt{\pi}} \exp\left\{-ik_x x_0 - \left[\frac{w_0 k_x}{2}\right]^2\right\} \tag{5.10}$$

and

$$E_{y,i}(k_x, z) = A_i^- \exp\{i\gamma_i(k_x)[z - z_{i+1}]\} + B_i^+ \exp\{-i\gamma_i(k_x)[z - z_i]\}, \tag{5.11}$$

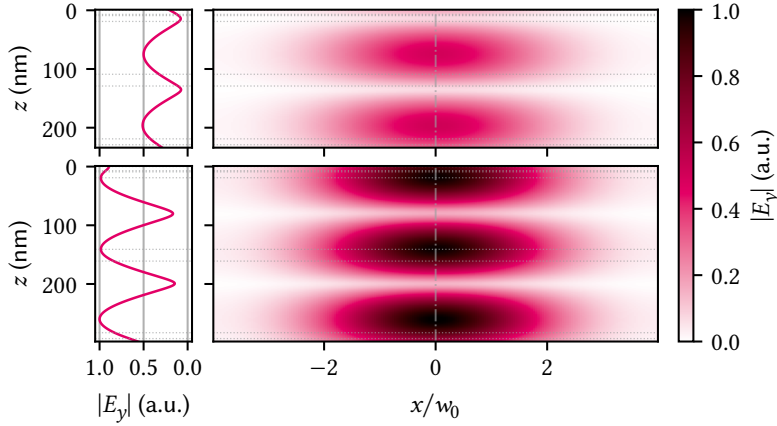3: *I. e.*, the inverse Fourier transform of $\mathcal{E}_0(k_x)E_{y,i}(k_x, z)$.

Figure 5.1: Absolute value of the electric field inside the double-gated heterostructure under illumination with a Gaussian beam at $\lambda = 825\,\mathrm{nm}$ from the top. Top (bottom) panels show the structure with the default (optimized) barrier thickness of $90\,\mathrm{nm}$ ($122\,\mathrm{nm}$), respectively. Dotted horizontal lines indicate interfaces between different materials while the vertical dash-dotted line indicates the position of the line cuts shown in the left column. Increasing the thickness of the barrier has two beneficial effects; first, the overall field intensity inside the structure is higher by a factor of two, and second, there is a peak rather than a knot in the QW at a depth of $\sim 120\,\mathrm{nm}$ ($\sim 150\,\mathrm{nm}$), leading to enhanced absorption.

and where we considered only normal incidence for simplicity.

In the second case, Langevin et al. [11] consider an AC current I flowing through a translationally invariant, one-dimensional wire along y at $x = x_{\mathrm{s}}$. This introduces a source term into the Helmholtz equation Equation 5.1 which, upon Fourier transforming in x direction, leads to

$$\frac{\partial^2 \hat{E}_y}{\partial z^2} + \gamma_i^2 \hat{E}_y = -i\omega\mu_0 I\delta(z)\exp(ik_x x_{\mathrm{s}}). \tag{5.12}$$

The electric field $\hat{E}_{y,i}(k_x, z)$ is thus proportional to the Green's function of Equation 5.12 and can be obtained using a similar procedure as in the case of a distant source incident on the structure by matching the interface conditions. Performing the inverse Fourier transform by means of Equation 5.9 with constant weights, $\mathcal{E}_0(k_x) \equiv 1$, then yields the two-dimensional spatial distribution of the electric field, $E_{y,i}(x, z)$.

Table 5.1

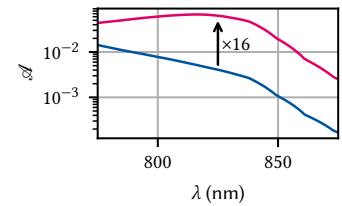|	$\mathscr{A}$ (%)	$\mathscr{R}$ (%)
Bare	2.93	22.43
TG	1.79	41.98
BG	0.50	82.72
TG+BG	0.41	84.78

Figure 5.2: QW absorptance $\mathscr{A}$ in a heterostructure with default (blue) and optimized (magenta) barrier thickness and top and bottom gates as function of wavelength. Optimization was performed at $825\,\mathrm{nm}$ using the differential evolution algorithm implemented in `PyMoosh`, resulting in a barrier thickness of $122\,\mathrm{nm}$ and an absorptance better by a factor of 16 at $6.3\,\%$.
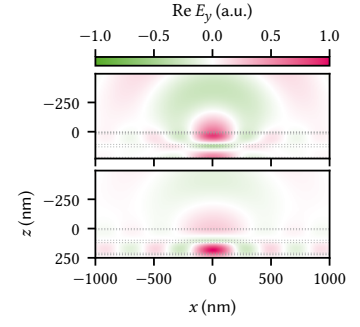
Figure 5.3: Real part of the electric field emitted by a current line located in the QW (black point) for different cases of the unoptimized structure. From top to bottom: bare heterostructure, top gate, bottom gate, top and bottom gate. The half space $z < 0$ is the air above the membrane in the direction of the objective lens and the dotted lines indicate interfaces between materials. Evidently, the bottom gate reduces the amplitude in the upper half of the membrane and thereby the outcoupling efficiency compared to the structures with just a top gate, consistent with what is observed in the experiment.
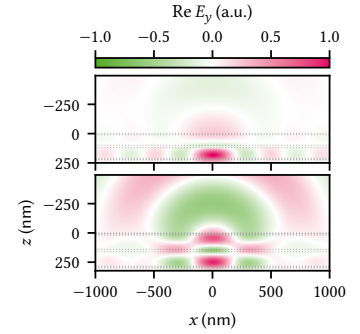

Figure 5.4: Real part of the electric field emitted by a current line located in the QW (black point) for the default (top) and optimized (bottom) structures with top and bottom gates. Optimizing the barrier thickness for absorption in the QW evidently also drastically improves the outcoupling efficiency into the halfspace $z < 0$.
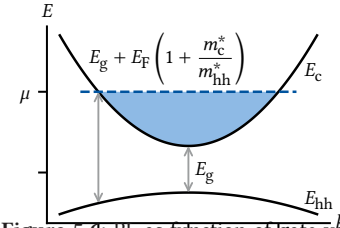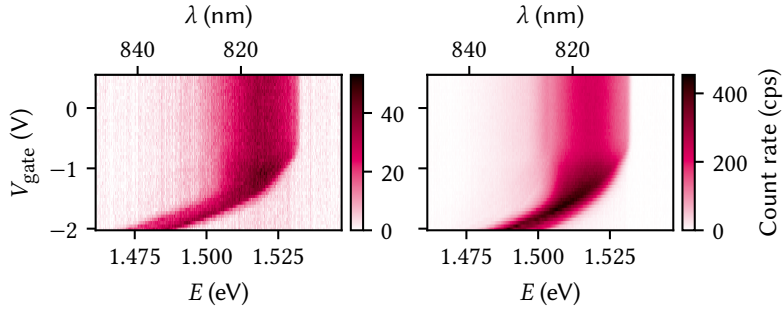
Figure 5.6: PL as function of gate voltage on a single fan-out gate on the bottom (left) and top (right) side of the membrane. The behavior is qualitatively similar but the overall quantum efficiency lower by an order of magnitude for gates on the bottom (as-grown buried) side.
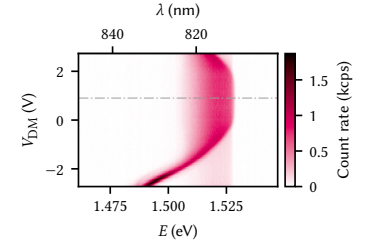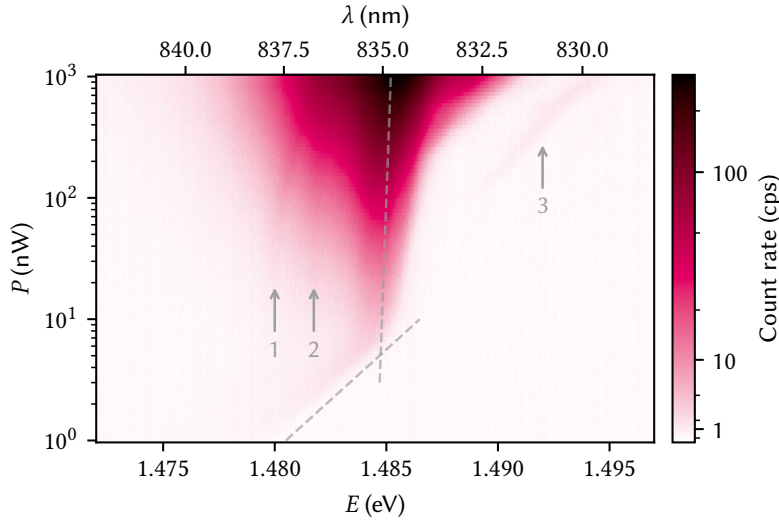
Figure 5.7: PL as function of difference-mode voltage on a large exciton trap. The observed Stark shift follows the expected quadratic dispersion, but is offset by 0.9 V with respect to zero bias (dash-dotted gray line). Remnant PL of the two-dimensional electron gas (2DEG) from outside the trap region is faintly visible below -1 V.
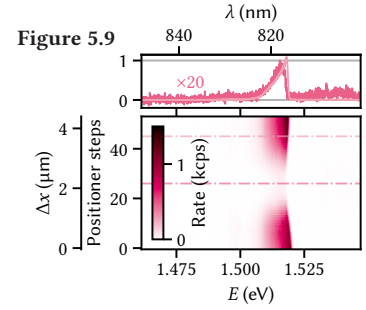
Figure 5.9

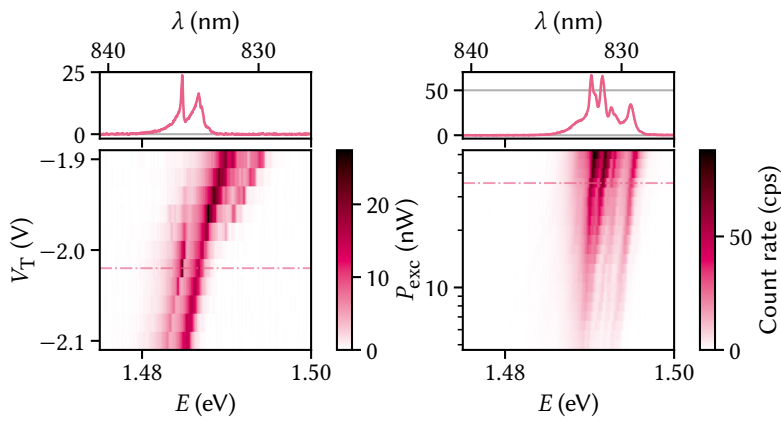**Figure 5.8**

Figure 5.10

Conclusion & outlook 6

D^{OGS}

Part IV

A Filter-Function Formalism For Unital Quantum Operations

APPENDIX

Additional TMM simulations

A.1 Dependence on epoxy thickness

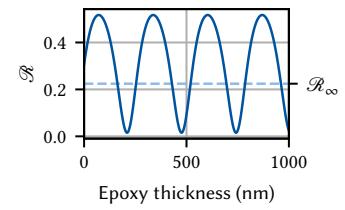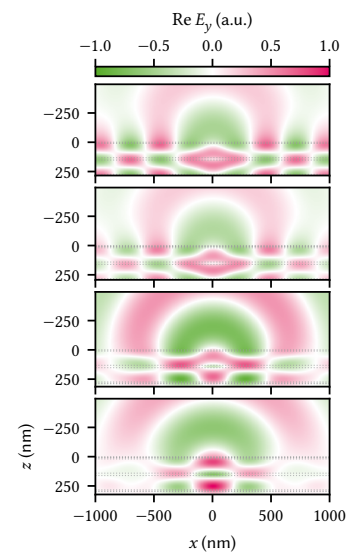## A.2 Optimization of the barrier thickness

Figure A.1

Figure A.2

Bibliography

[1] D. Kamburov et al. "Use of Micro-Photoluminescence as a Contactless Measure of the 2D Electron Density in a GaAs Quantum Well." In: *Appl. Phys. Lett.* 110.26 (June 26, 2017), p. 262104. DOI: 10.1063/1.4985439. (Visited on 06/29/2022) (cited on page 15).

[2] R. C. Miller, D. A. Kleinman, and A. C. Gossard. "Energy-Gap Discontinuities and Effective Masses for GaAs − $Al_x Ga_{1-x}$As Quantum Wells." In: *Phys. Rev. B* 29.12 (June 15, 1984), pp. 7085–7087. DOI: 10.1103/PhysRevB.29.7085. (Visited on 06/30/2022) (cited on page 16).

[3] A. Rabinovitch and J. Zak. "Electrons in Crystals in a Finite-Range Electric Field." In: *Phys. Rev. B* 4.8 (Oct. 15, 1971), pp. 2358–2370. DOI: 10.1103/PhysRevB.4.2358. (Visited on 06/26/2025) (cited on page 16).

[4] D. A. B. Miller et al. "Electric Field Dependence of Optical Absorption near the Band Gap of Quantum-Well Structures." In: *Phys. Rev. B* 32.2 (July 15, 1985), pp. 1043–1060. DOI: 10.1103/PhysRevB.32.1043. (Visited on 06/30/2022) (cited on pages 16, 17).

[5] John H. Davies. *The Physics of Low-Dimensional Semiconductors: An Introduction*. Cambridge: Cambridge Univ. Press, 2009. 438 pp. (cited on pages 16–18).

[6] Thomas Descamps. "Electrostatic Exciton Trap in a Thin Semiconductor Membrane for Optical Coupling to a GaAs Spin Qubit." PhD thesis. Aachen: RWTH Aachen University, 2021 (cited on pages 17, 18).

[7] A. V. Kavokin. "Exciton Oscillator Strength in Quantum Wells: From Localized to Free Resonant States." In: *Phys. Rev. B* 50.11 (Sept. 15, 1994), pp. 8000–8003. DOI: 10.1103/PhysRevB.50.8000. (Visited on 07/17/2025) (cited on pages 17, 18).

[8] Thomas Olsen et al. "Simple Screened Hydrogen Model of Excitons in Two-Dimensional Materials." In: *Phys. Rev. Lett.* 116.5 (Feb. 2, 2016), p. 056401. DOI: 10.1103/PhysRevLett.116.056401. (Visited on 07/16/2025) (cited on page 17).

[9] E. Karimi et al. "Radial Quantum Number of Laguerre-Gauss Modes." In: *Phys. Rev. A* 89.6 (June 16, 2014), p. 063813. DOI: 10.1103/PhysRevA.89.063813. (Visited on 07/17/2025) (cited on page 18).

[10] Robert C. Hilborn. "Einstein Coefficients, Cross Sections, f Values, Dipole Moments, and All That." In: *Am. J. Phys.* 50.11 (Nov. 1, 1982), pp. 982–986. DOI: 10.1119/1.12937. (Visited on 07/16/2025) (cited on page 18).

[11] Denis Langevin et al. "PyMoosh: A Comprehensive Numerical Toolkit for Computing the Optical Properties of Multilayered Structures." In: *J. Opt. Soc. Am. B* 41.2 (Feb. 1, 2024), A67. DOI: 10.1364/JOSAB.506175. (Visited on 11/11/2024) (cited on pages 20–22).

[12] Denny Dütz et al. "Distributed Bragg Reflectors for Thermal Isolation of Semiconductor Spin Qubits." In preparation (cited on page 21).

[13] A. D'Andrea and R. Del Sole. "Exciton Quantization and Polariton Propagation in Semiconductor Slabs: From Semi-Infinite Crystals to Quantum Wells." In: *Phys. Rev. B* 41.3 (Jan. 15, 1990), pp. 1413–1423. DOI: 10.1103/PhysRevB.41.1413. (Visited on 07/17/2025) (cited on page 21).

Special Terms

Numbers
2DEG two-dimensional electron gas. 25

C
CCD charge-coupled device. 19

P
PL photoluminescence. 16, 20, 24, 25

Q
QCSE quantum-confined Stark effect. iii, 16–18
QW quantum well. 16–18, 22, 23

T
TE transverse electric. 20, 21
TMM transfer-matrix method. iii, 20, 21, 30

Declaration of Authorship

I, Tobias Hangleiter, declare that this thesis and the work presented in it are my own and has been generated by me as the result of my own original research.

I do solemnly swear that:

1. This work was done wholly or mainly while in candidature for the doctoral degree at this faculty and university;
2. Where any part of this thesis has previously been submitted for a degree or any other qualification at this university or any other institution, this has been clearly stated;
3. Where I have consulted the published work of others or myself, this is always clearly attributed;
4. Where I have quoted from the work of others or myself, the source is always given. This thesis is entirely my own work, with the exception of such quotations;
5. I have acknowledged all major sources of assistance;
6. Where the thesis is based on work done by myself jointly with others, I have made clear exactly what was done by others and what I have contributed myself;
7. Parts of this work have been published before as:

[1] Pascal Cerfontaine, Tobias Hangleiter, and Hendrik Bluhm. "Filter Functions for Quantum Processes under Correlated Noise." In: *Phys. Rev. Lett.* 127.17 (Oct. 18, 2021), p. 170403. DOI: 10.1103/PhysRevLett.127.170403.

[2] Thomas Descamps, Feng Liu, Tobias Hangleiter, Sebastian Kindel, Beata E. Kardynał, and Hendrik Bluhm. "Millikelvin Confocal Microscope with Free-Space Access and High-Frequency Electrical Control." In: *Rev. Sci. Instrum.* 95.8 (Aug. 9, 2024), p. 083706. DOI: 10.1063/5.0200889. (Visited on 08/12/2024).

[3] Tobias Hangleiter, Pascal Cerfontaine, and Hendrik Bluhm. "Filter-Function Formalism and Software Package to Compute Quantum Processes of Gate Sequences for Classical Non-Markovian Noise." In: *Phys. Rev. Research* 3.4 (Oct. 18, 2021), p. 043047. DOI: 10.1103/PhysRevResearch.3.043047. (Visited on 01/19/2022).

[4] Tobias Hangleiter, Pascal Cerfontaine, and Hendrik Bluhm. "Erratum: Filter-function Formalism and Software Package to Compute Quantum Processes of Gate Sequences for Classical Non-Markovian Noise [Phys. Rev. Research 3, 043047 (2021)]." In: *Phys. Rev. Res.* 6.4 (Oct. 16, 2024), p. 049001. DOI: 10.1103/PhysRevResearch.6.049001. (Visited on 10/16/2024).

Aachen, July 18, 2025.